Signal-to-noise ratio in lock-in amplifier synchronous detection: A generalized communications systems approach with applications to frequency, time, and hybrid (rate window) photothermal measurements

Andreas Mandelis
Photothermal and Optoelectronic Diagnostics Laboratory and Manufacturing Research Corporation of Ontario, Department of Mechanical Engineering, University of Toronto, Toronto, Ontario M5S 1A4, Canada

(Received 1 March 1994; accepted for publication 4 August 1994)

Detailed analytical models of signal-to-noise ratios (SNR) of the conventional frequency domain (FD) and time domain (TD) photothermal measurement methodologies are developed and compared to the rate-window photothermal method, both theoretically and experimentally. The conclusions of this study demonstrate that the lock-in amplifier (LIA) rate-window measurement mode in general, and the digital LIA mode, in particular, exhibits superior SNR to both the conventional frequency-scanned LIA FD method and to the transient, time-averaged TD method. Between the pulse-duration-scanned and pulse-repetition-period scanned rate-window methodologies, the former clearly exhibits superior SNR. The theoretical conclusions are in agreement with experimental SNRs using the implementation of the foregoing measurement methodologies with simple infrared photothermal radiometric setups.

I. INTRODUCTION

Photothermal rate-window detection[1] has proven to be very effective in the measurement of thermal diffusivities of ultrahigh thermal conductors such as diamonds[2] and of electronic carrier recombination lifetimes in the presence of deep-level defects.[3,4] An experimental comparison between the conventional frequency-domain (FD) infrared photothermal radiometric method and the lock-in amplifier (LIA) rate-window method using an identical setup was recently performed.[5] That study concluded experimentally that the rate-window method gives superior signal-to-noise ratio (SNR) for materials with very short thermal transport times such as metal foils, which otherwise require high-frequency FD scans with low SNR. The rate-window measurement SNR became substantially superior to the FD measurement SNR with increased thermal-wave modulation frequency, especially in the pulse duration scanned mode. Furthermore, it has been shown[2] that the LIA rate-window SNR is superior to that resulting from a boxcar integrator. The two SNRs become equal as the boxcar detection approaches monotonically the lock-in SNR when the boxcar time-gate width increases towards $T_0/2$. Here T_0 is the transient signal repetition period. The foregoing comparisons between the photothermal LIA and boxcar integrator rate-window methods[2] showed that the SNR of the former is approximately a factor of two better, a fact supported by Miller *et al.*[6] in studies of the relative SNR performance of these two methods as applied to the well-known semiconductor diagnostic technique called deep-level transient spectroscopy (DLTS).

In view of the increasing body of evidence regarding the SNR advantages of rate-window photothermal measurements over the conventional FD and TD techniques, a complete theoretical study of this parameter was undertaken in this work, backed by the appropriate experimental results. To the author's best knowledge the existing literature on lock-in analyzer instrumentation analysis and signal generation is concentrated in the presentation of dynamic aspects of specific detection principles [e.g., heterodyne lock-in amplifiers,[7,8] pulsewidth modulation (PWM) lock-in amplifiers[9]] or in mainly qualitative descriptions of the general lock-in configurations originating in phase-sensitive detectors.[10] The most comprehensive treatise on lock-in amplifier principles and applications has been written by Meade;[11] although some quantitative SNR results were presented, the approach was mostly practical and qualitative with emphasis on component design, specialized circuit configurations, and applications using lock-in detection. Conversely, an excellent treatise on signal recovery from noise with mathematical considerations of the effects of various filters has been presented by Wilmshurst.[12] His treatment includes a very clear diagrammatic presentation of the frequency-domain view of the phase-sensitive detector (PSD), the principle on which LIA operation is based. Unfortunately, the actual treatment of the LIA, which requires the presence of a low-pass filter (LPF) past the PSD stage, is qualitative and does not generate a thorough understanding of the instrument's operation.

The most rigorous study of electronic signals, noise, and measurement analysis to date using a communications systems approach has been presented by Cova and Longoni.[13] These authors have outlined the theoretical foundations of the various measurement techniques and signal processing

 0034-6748/94/65(11)/3309/15/$6.00

methods from the fundamental viewpoint of deterministic and random variables, signals, noise, and background. The mathematical and physical aspects of linear filtering methods for the extraction of signals from noise have been treated including the important topic of optimum filtering. In the context of Cova and Longoni's work, the LIA was discussed qualitatively as a common example of a correlation filter, or PSD, but no specific SNR analysis was given. In many ways it is surprising that no rigorous generalized mathematical formulation of lock-in signal and SNR has been developed to the present. This state of affairs may be largely attributed to the fact that most of the developments in this area have been made in industrial laboratories, in which the emphasis was (and still is) on the relative instrumental advantages of specialized lock-in analyzers over other existing commercial instruments. As a consequence, the existing technical manuals are based on specialized circuitry and practical demonstrations, at the expense of a generalized, unified signal processing approach. Similarly, the systems aspects of lock-in amplifiers have been confined, for the most part, to the manufacturer's data sheets and application notes.[11]

In this review article, a generalized communications systems approach to signal and noise processing by the basic circuit of two-phase lock-in amplifiers has been developed. The resulting general SNR expressions were then applied to rate window and FD modes in the specific case of photothermal signal generation. Finally, detailed comparisons with time-averaged transient photothermal SNRs were made under conditions which allow the direct comparison among all three signal generation modes. Even though the nature of the following presentation is of a review type, the resulting LIA SNR expressions are largely new, including the photothermal signal SNRs as well as several experimental results.

II. LOCK-IN AMPLIFIER OUTPUT SIGNAL

A. Qualitative

Multiple time averaging (MTA) and LIA filtering are routinely used in signal processing as effective techniques reducing instrumental drift error and background white noise, mainly thermal and shot noise. In MTA using repetitive pulses leading to signal transients it is well-known[12] that, if the number of signal traces averaged is n_t, the amount of time available for noise averaging is increased by the factor n_t and the final error for each of the transient data points decreases by $n_t^{-1/2}$, thus offering a similar noise improvement to the MTA TD signal. In Sec. IV C it will be shown that as the number of signal traces increases to infinity, one obtains the mean value of the signal over the frequency bandwidth of the signal processing instrumentation. Given that this bandwidth must, by necessity, be broad enough to pass the Fourier components of the generated signal relatively undistorted, it is intuitively easy to see the built-in SNR advantage of narrow-band detection such as that afforded by LIAs. The main strengths of MTA, therefore, lie in drift error correction of signal base lines[12] and in the powerful simplifications of physical interpretations associated with the time evolution of physical TD signal generation processes, compared to time-multiplexed FD scans.

Furthermore, LIA detection has the distinct advantage of depending on PSD operation which itself tends to reject drift. In addition, the possibility of using ac-coupled signal amplification stages (rather than the dc-coupled MTA amplifier) can act as an effective filter to drift. Owing to the LPF stage of the LIA, extremely narrow-band detection can be realized, so that white noise rejection can be far superior to MTA noise output, leading to much higher SNR. Wilmshurst[12] has given a thorough discussion of the relative MTA/LIA behaviors in reducing or eliminating $1/f$ noise error. Although the treatment of this type of noise is beyond the scope of the present review, its main characteristic is that, unlike white noise which has a zero mean, $1/f$ noise has the tendency to wander away from the mean. Therefore, the advantages of using a larger measurement period T are less than for white noise. Wilmshurst[12] has shown that both MTA and PSD (LIA) methods can, in principle, effectively remove $1/f$ noise error. Nevertheless, there appear to be more severe practical limitations with the MTA method, mainly associated with large time interval T. Of course, the white-noise reduction advantages of the LIA remain after (hypothetically) all $1/f$ components have been removed from both MTA and FD methods (Sec. III).

Beyond the LIA SNR advantages over the TD MTA scheme, there exist further "intra-FD" SNR advantages regarding the LIA rate-window signal generation mode, compared to harmonic (i.e., 50% duty cycle) inputs to the LIA. One can generate LIA rate-window scans simply by continuously varying the duty cycle over one signal repetition period. This can be done either by pulse duration τ_p or by pulse repetition period T_0 scans. The result is that, instead of the conventional sinusoidal or square-wave system generation and LIA detection, an entire repetitive transient is sampled by the LIA each T_0.

Qualitatively, the SNR advantage of this mode can be understood by considering that the lock-in amplifier captures the signal energy contained in the first (fundamental) Fourier coefficient of the rate-window transient; accordingly, in the FD case it monitors the fundamental Fourier coefficient of the harmonic signal. To focus attention to a specific signal generation process, it is well-known from time- and frequency-domain analyses of photothermal signals that in the thermal transient the optically imparted energy distributes itself in such a manner that it provides the strongest response at times immediately following the pulse cutoff. This is, precisely, the range of scanned times involved in the rate-window technique which therefore yields a strong fundamental coefficient magnitude of the Fourier series representation of the repetitive pulse. Conversely, in harmonic photothermal analysis the fundamental Fourier coefficient of the repetitive 50% duty cycle pulse decreases in magnitude in inverse proportion to the strength of the first Fourier coefficient of the time-domain pulse, due to the inverse relationship between time- and frequency-domain and the Parseval theorem.[13] Therefore, fast photothermal phenomena are expected to yield fundamental Fourier coefficients of superior strength in the transient repetitive pulse mode to the one allotted to the respective high frequency fundamental component under harmonic excitation, and the higher the fre-

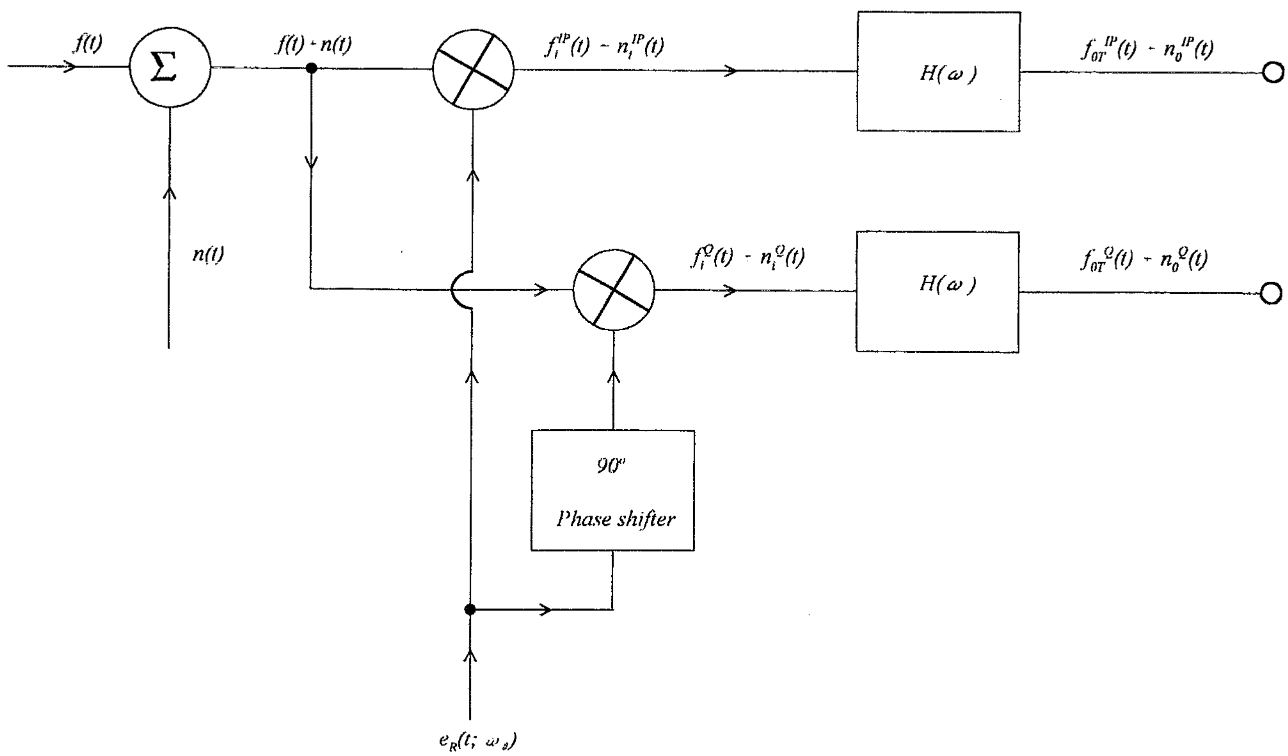

FIG. 1. Layout of transient signal pathway through a lock-in amplifier (LIA). The various symbols are defined in the text. Σ represents summing stage and × represents mixing (multiplying) stage.

quency, the higher the strength contrast of the fundamentals in the two transform domains. The result is, of course, higher SNR for the transient response (commonly observed as a strong early-time response of pulsed laser photothermal systems[2]). Similar arguments concerning nonphotothermal systems can be made based on the nature of the basic Fourier transform pair. A detailed theoretical analysis of the foregoing qualitative discussion will be presented in Sec. IV.

B. Quantitative

An experimental detection system using lock-in filtering is illustrated in Fig. 1. An input time-dependent (nonstationary) signal $F(t)$ in the presence of noise $n(t)$ is multiplied with a reference wave form $e_R(t;\omega_0)$ and introduced into the low-pass filter of transfer function $H(\omega)$. In the case of a two phase/vector LIA there exists a second channel, the reference phase of which is shifted by 90° with respect to $e_R(t;\omega_0)$. The output of the mixer of this stage is introduced to an identical low-pass filter $H(\omega)$. The two outputs constitute the in-phase (IP) and quadrature (Q) components of the LIA signal, respectively. All lock-in detection schemes can be decomposed into the basic system structure shown in Fig. 1.[14–17] Since the output signal $f(t)$ is periodic with period T_0 corresponding to reference angular frequency $\omega_0 = 2\pi/T_0$, the output power SNR is given as[18]

$$\mathrm{SNR} = \frac{\text{average spectral power of signal output}}{\text{average spectral power of noise output}}, \tag{1}$$

$$= \frac{\overline{P(t)}}{\overline{P_n(t)}}. \tag{2}$$

The experimental recorded SNR is simply the square root of the power SNR of Eq. (1). It is appropriate to use the mean-square value of the noise amplitude, since it is a random signal with zero mean value. The periodic output signal $f_0(t)$ can be decomposed into a Fourier series. It is convenient to use the complex series expansion

$$f_0(t) = \sum_{n=-\infty}^{\infty} \phi_n e^{in\omega_0 t}, \tag{3}$$

because it includes "negative frequency" components, which can be interpreted as the low-passband components below the dc-shifted filter bandwidth center of the LIA. The Fourier transform of the output signal is

$$\tilde{F}_0(\omega) = 2\pi \sum_{n=-\infty}^{\infty} \phi_n \delta(\omega - n\omega_0), \tag{4}$$

where δ is the Dirac delta function defined in the particular representation

$$\delta(\omega) = \lim_{k\to\infty}\left(\frac{k}{\pi} Sa^2(k\omega)\right), \tag{5}$$

$Sa(x)$ is the sampling function[18]

$$Sa(x) = \frac{\sin x}{x}. \tag{6}$$

Owing to the fact that $f_0(t)$ becomes aperiodic by truncating it outside the interval $t<T$ where T is some time interval $T\rightarrow\infty$

$$f_{0T}(t)=\begin{cases} f_0(t); & 0<t<T \\ 0; & t<0 \end{cases}, \tag{7}$$

it can be shown that the Fourier transform of $f_{0T}(t)$ is

$$\tilde{F}_{0T}(\omega)=T_0 \sum_{n=-\infty}^{\infty} \phi_n Sa\left(\frac{(\omega-n\omega_0)T}{2}\right). \tag{8}$$

From the definition of the power spectral density (PSD)[18]

$$\mathrm{PSD}[f_{0T}(t)]\equiv S_F(\omega)=\lim_{T\rightarrow\infty}\frac{|\tilde{F}_{0T}(\omega)|^2}{T}. \tag{9}$$

Use of the definition (5) for the Dirac delta function immediately gives

$$S_F(\omega)=2\pi \sum_{n=-\infty}^{\infty} |\phi_n|^2\delta(\omega-n\omega_0). \tag{10}$$

Equation (10) indicates that the available signal power at the outputs of the LIA, either the IP or Q channel, is distributed throughout the discrete spectrum of the fundamental and the harmonics of the reference angular frequency ω_0.

Assuming a single first-order RC low-pass filter section of transfer function[11,14]

$$H(\omega)=\frac{1}{1+i\omega\tau_{\mathrm{RC}}}, \tag{11}$$

keeps the treatment quite general, as various higher order filter gain roll-offs can be implemented by simple single filter section cascades using buffer amplifiers for isolation.[11] Here $\tau_{\mathrm{RC}}=\mathrm{RC}$ (R: resistance, C: capacitance of the filter). The impulse response of the filter is given by the inverse Fourier transform of Eq. (11)

$$h(t)=\frac{1}{\tau_{\mathrm{RC}}}e^{-t/\tau_{\mathrm{RC}}}u(t), \tag{12}$$

where $u(t)$ is the unit step function. The filter output $f_{0T}(t)$ is the result of the convolution[12]

$$\begin{aligned} f_{0T}(t)&=\int_{-\infty}^{\infty} h(t-\zeta)f_i(\zeta)d\zeta \\ &=\frac{e^{-t/\tau_{\mathrm{RC}}}}{\tau_{\mathrm{RC}}}\int_{-\infty}^{t} f_i(\zeta)e^{\zeta/\tau_{\mathrm{RC}}}d\zeta. \end{aligned} \tag{13}$$

According to Eq. (13) $f_{0T}(t)$ is the time average of the intermediate $f_i(t)$ stage computed over the time interval $\tau_{\mathrm{RC}}\gg T_0$ assuming the LIA filter time constant to be very long compared to T_0 (the usual experimental situation). Since $f_i(t)$ contains a dc component and harmonics of ω_0, this average can be simply taken over the period T_0. Operationally, since $f_i(t)$ is subject to the aperiodic truncation of Eq. (7)

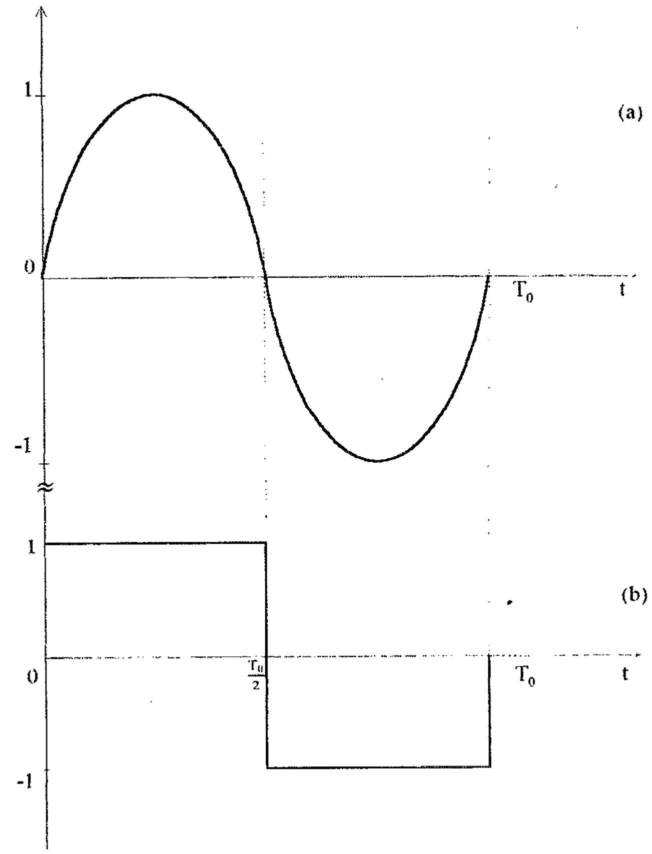

FIG. 2. Reference wave forms for LIA: (a) digital, and (b) analog instrument. Both phases were assumed 0° at $t=0$.

$$\begin{aligned} f_{0T}&\simeq\frac{1}{\tau_{\mathrm{RC}}}\int_0^T f_i(\zeta)d\zeta \\ &\simeq\lim_{T\rightarrow\infty}\frac{1}{T}\int_0^T f_i(\zeta)d\zeta\simeq\frac{1}{T_0}\int_0^{T_0} f_i(\zeta)d\zeta=f_{0T}(T_0). \end{aligned} \tag{14}$$

One arrives at the form of Eq. (14) by expanding the exponentials in Eq. (13) on the basis of $t\ll\tau_{\mathrm{RC}}$ and redefining the long time interval T to coincide with the long time constant τ_{RC} of the filter. If the condition $t\ll\tau_{\mathrm{RC}}$ is not valid, $f_{0T}(t)$ must be used from Eq. (13) and the LIA output remains time dependent, an easy to verify, yet not very useful experimental fact.[1] At this point it should be remembered that $f_i(t)$ is the output of the IP or Q mixer stage. Therefore, it consists of the product of the input transient wave form $f(t)$ and the reference wave form $e_R(t;\omega_0)$. Depending on the type of LIA used, two reference wave forms can be considered. In digital instruments the reference is a pure sine wave synthesized digitally. In analog instruments a square wave reference signal is used (Fig. 2).

1. Digital LIA signal

Digital LIAs were inspired from early instrumentation using digital synchronous detection by means of a single reversible scaler developed for single-photon detection[19]; its

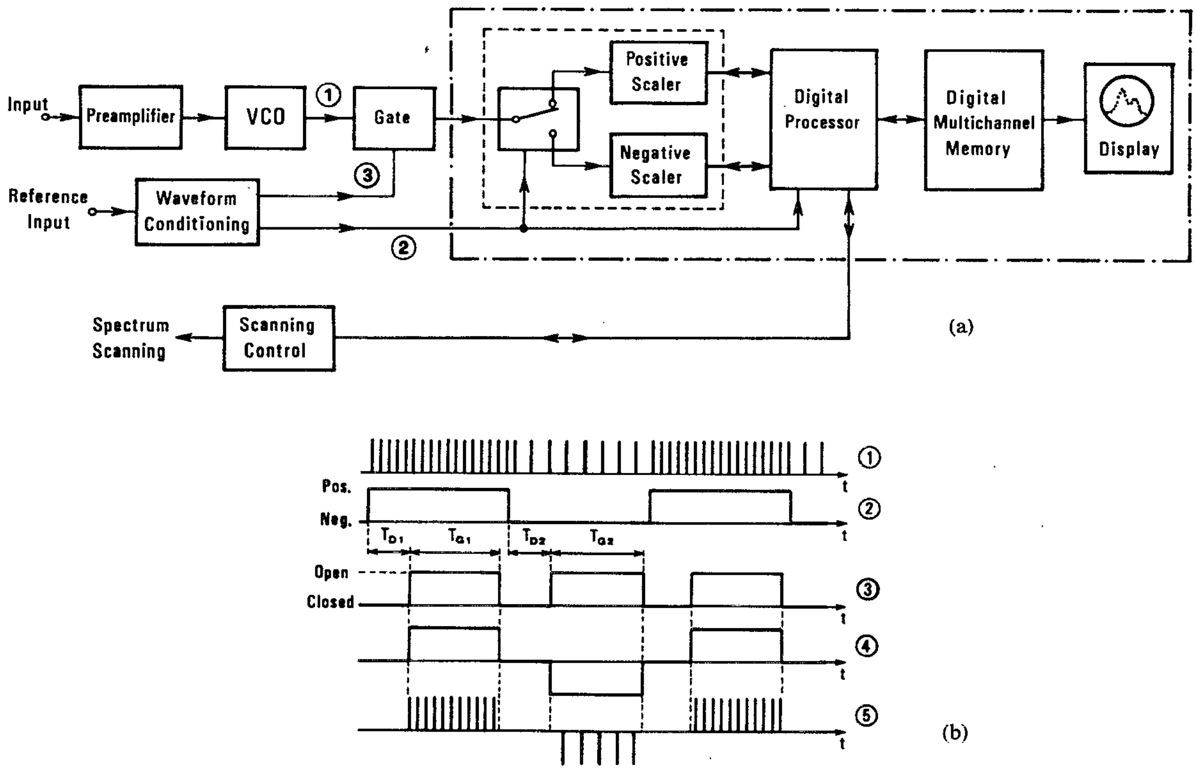

FIG. 3. (a) Functional block diagram of the digital lock-in detection technique (Ref. 22). (b) Principal waveforms in (a) for the case of square-wave modulation (optical choppers etc.); (1) Voltage-controlled oscillator (VCO) output; (2) Switch driving the binary wave form synchronized to the reference signal; (3) Gate-opening binary wave form, also synchronized to the reference signal; (4) Equivalent weighting wave form of the PSD; and (5) PSD output.

extension to analog signals by using a voltage-to-frequency converter was devised for various applications.[20,21] Later on, a pioneering digital LIA was reported by Cova *et al.*[22] The main purpose of the novel LIA was to overcome many practical limitations of the analog LIAs of the day and pointed out the basic advantages of digital demodulation, primarily the more efficient cutoff of the low-frequency noise components even with a square-wave reference function. Of particular concern was the measurement of low-frequency signals, the rejection of unwanted dc and low-frequency components, and the overall enhancement of the SNR especially in the presence of source intensity drifts. Figure 3 shows the block diagram and principal wave forms of the digital LIA introduced by Cova *et al.*[22] A major advantage of that instrument of direct relevance to the present analysis was its ability to exhibit perfect gated integration through counting performed by positive or negative scalers preceding the digital processor (Fig. 3) and following a gated precision voltage-controlled oscillator (VCO) acting as a linear voltage-to-frequency converter. As a result, the digital PSD (gate plus switch) exhibited an equivalent weighting wave form with a very accurately nulled average value. The use of the gate allowed the LIA to be very versatile, operating with high accuracy in a variety of cases and with different weighting wave forms, not restricted to the conventional analog LIA square waves having 50% duty cycle. Besides the square wave filtering/reference wave form at the fundamental modulation frequency f_R, practically any other filtering type could be well-approximated by synthesizing suitable, pulse-width modulated square waves at higher frequencies. For instance,[22] filtering at f_R could be obtained by subdividing the gating time in shorter intervals and by opening the gate (Fig. 3) only for a fraction of each interval modulated by the fundamental sinusoidal component of the reference. As a result, this operating mode became very useful in synthesizing accurate narrow-band filtering *free from unwanted harmonic bands*, even at low frequencies, as shown below. Furthermore, the digital LPF can have practically unlimited integration time τ_{RC} and it is free from internal noise sources to which analog filters are susceptible. Greater SNR can thus be obtained.

In terms of the generalized signal processing analysis of the digital LIA, Fig. 1 remains the preferred instructional alternative. Equation (14) may be written

$$f_{0T}^{(\mathrm{IP,Q})}(T_0)=\frac{1}{T_0}\int_0^{T_0} f(\zeta)e_R^{(\mathrm{IP,Q})}(\zeta;\omega_0)d\zeta, \tag{15}$$

for either the IP or Q signal channel, where

$$e_R^{\mathrm{IP}}(t;\omega_0)=\cos(\omega_0 t), \tag{16a}$$

$$e_R^{\mathrm{Q}}(t;\omega_0)=\sin(\omega_0 t). \tag{16b}$$

The repetitive input transient $f(t)$ may be expanded in a real Fourier series

$$f(t)=\frac{1}{2}a_0+\sum_{n=1}^{\infty}[a_n\cos(n\omega_0 t)+b_n\sin(n\omega_0 t)], \tag{17a}$$

with the well-known Fourier coefficients[23]

$$a_n(\omega_0)=\frac{\omega_0}{\pi}\int_0^{T_0}f(t)\cos(n\omega_0 t)dt, \tag{17b}$$

and

$$b_n(\omega_0)=\frac{\omega_0}{\pi}\int_0^{T_0}f(t)\sin(n\omega_0 t)dt. \tag{17c}$$

The orthogonality property of the basis functions $\{\cos(n\omega_0 t)\}$ and $\{\sin(n\omega_0 t)\}$ yields upon combination of Eqs. (15)–(17)

$$f_{0T}^{(\mathrm{IP,Q})}(\omega_0)=\frac{1}{2}\begin{bmatrix}a_1(\omega_0)\\ b_1(\omega_0)\end{bmatrix}. \tag{18}$$

Equation (18) represents the demodulated (dc) output components of the IP and Q channels, respectively. It should be noticed that, although these are dc-level signals, the waveform constituents $f(t)$ used in the integrations (15) carry a ω_0 dependence owing to the repetitive nature of the wave form with period T_0. This cutoff parameter renders $f(T_0)$ the extreme value of $f(t)$ in the time evolution of the wave form and is central in the location of the extremum in the diagnostic technique of the LIA rate window.[1,6,24,25] Identification of the coefficients $a_1/2, b_1/2$ with the $n=0$ components of the complex Fourier expansion, Eq. (3), gives for the PSD of the output signal

$$S_{\mathrm{F}}^{\mathrm{IP}}(\omega;\omega_0)=\frac{\pi}{4}|a_1(\omega_0)|^2\delta(\omega), \tag{19a}$$

$$S_{\mathrm{F}}^{\mathrm{Q}}(\omega;\omega_0)=\frac{\pi}{4}|b_1(\omega_0)|^2\delta(\omega). \tag{19b}$$

Equation (19) may be used to calculate the average output spectral power[18]

$$\bar{P}=\lim_{T\to\infty}\int_{-T/2}^{T/2}f^2(t)dt=\frac{1}{2\pi}\int_{-\infty}^{\infty}S_F(\omega;\omega_0)d\omega. \tag{20}$$

Therefore,

$$\bar{P}_d^{(\mathrm{IP,Q})}(\omega_0)=\frac{1}{8}\begin{bmatrix}|a_1(\omega_0)|^2\\ |b_1(\omega_0)|^2\end{bmatrix}\quad[W]. \tag{21}$$

It is important to note that the signal output from a digital lock-in amplifier contains no harmonic components, precisely due to the purely sinusoidal reference.[17] This is an advantage, because it eliminates noise contributions from harmonic responses, compared to analog LIAs.[22]

2. Analog LIA signal

The generalized schematic of Fig. 1 is valid for analog LIAs as well.[14] Here assume the reference wave form shown in Fig. 2(b). Equation (15) now gives

$$f_{0T}^{\mathrm{IP}}(T_0)=\int_0^{T_0/2}f(\zeta)(+1)d\zeta+\int_{T_0/2}^{T_0}f(\zeta)(-1)d\zeta$$
$$=\int_0^{T_0/2}f(\zeta)d\zeta-\int_{T_0/2}^{T_0}f(\zeta)d\zeta. \tag{22}$$

In terms of the Fourier components of $f(t)$ a straightforward calculation shows that

$$f_{0T}^{\mathrm{IP}}(\omega_0)=\frac{2}{\pi}\sum_{n=1}^{\infty}\frac{1}{2n-1}b_{2n-1}(\omega_0), \tag{23}$$

where the indicated ω_0 dependence of the output dc-level signal appears for the reason discussed earlier regarding the digital LIA output, Eq. (18). Similarly,

$$f_{0T}^{\mathrm{Q}}(T_0)=-\int_0^{T_0/4}f(\zeta)d\zeta+\int_{T_0/4}^{3T_0/4}f(\zeta)d\zeta-\int_{3T_0/4}^{T_0}f(\zeta)d\zeta, \tag{24}$$

which yields

$$f_{0T}^{\mathrm{Q}}(\omega_0)=-\frac{2}{\pi}\sum_{n=1}^{\infty}\frac{1}{2n-1}a_{2n-1}(\omega_0). \tag{25}$$

It can be seen that the well-known fact of the existence of all odd harmonics of the reference frequency results in an *apparent* improvement in signal output of the analog LIA compared to the single-component digital counterpart. Using Eqs. (10) and (20) one can obtain the average output spectral power for the analog LIA

$$\bar{P}_a^{\mathrm{IP}}(\omega_0)=\frac{1}{16}\left|\sum_{n=1}^{\infty}\frac{1}{2n-1}b_{2n-1}(\omega_0)\right|^2\quad[W], \tag{26a}$$

and similarly

$$\bar{P}_a^{\mathrm{Q}}(\omega_0)=\frac{1}{16}\left|\sum_{n=1}^{\infty}\frac{1}{2n-1}a_{2n-1}(\omega_0)\right|^2\quad[W]. \tag{26b}$$

A comparison with $\bar{P}_d(\omega_0)$, Eq. (21) shows that the apparent signal advantage of the analog LIA consists of coherent contributions of higher harmonics, which are nevertheless eliminated from the output in practice due to odd harmonic filtering (see Sec. IV A 2). The signal-to-noise ratio actually decreases, because all odd harmonics present in Eq. (26) contribute to the noise, as will be seen in Sec. III.

III. LOCK-IN AMPLIFIER OUTPUT NOISE

The most commonly encountered noise in instrumentation systems is the so-called Gaussian noise. This type of noise is characterized by zero mean and a Gaussian probability density function. Considering a LIA input noise signal $n(t)$ with power spectral density $S(\omega)$, we may conveniently represent[26] $n(t)$ as the limit of a sum of sinusoids of frequency Δf apart over its frequency spectrum, when $\Delta f\to 0$. Therefore,

$$n(t)=\lim_{\Delta\omega\to 0}\sum_{j=-\infty}^{\infty}C_j\cos(\omega_j t+\theta_j);\quad \omega_j=j\Delta\omega, \tag{27}$$

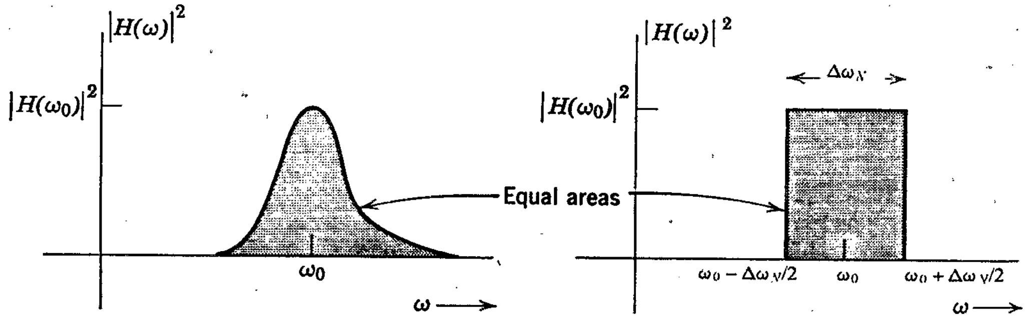

FIG. 4. Definition of the equivalent noise bandwidth (ENBW) of LIA.

where the Fourier coefficient C_j is to be determined. Upon passage through the LIA filter of transfer function $H(\omega)$, the mean-square value of the output noise is

$$\overline{n_0^2(t)}=\frac{1}{2\pi}\int_{-\infty}^{\infty} S_i(\omega)|H(\omega)|^2 d\omega, \tag{28}$$

where $S_i(\omega)$ is the power spectral density of the intermediate stage noise, $n_i(t)$, in Fig. 1. In fact, the modulation signal $e_R(t;\omega_0)$ makes the intermediate noise $n_i(t)$ *not* stationary, even with a stationary input noise $n(t)$. Nevertheless, the output noise $n_0(t)$ is stationary owing to the presence of the LPF. This filter allows only the low-frequency components of $S_i(\omega)$ to contribute to the output noise within its equivalent noise bandwidth $\Delta\omega_N$ (see below). The LPF averages over several modulation periods consistently with its τ_{RC} and outputs a stationary $n_0(t)$, i.e., with a mean-square value independent of t. For each Fourier component of $n(t)$ in Eq. (27), a treatment similar to that of the periodic output signal $f_0(t)$, Eqs. (3)–(10) gives for the input noise PSD the discretized power spectrum

$$S(\omega)=2\pi \lim_{\Delta\omega\to 0}\sum_{j=-\infty}^{\infty}\left|\frac{C_j}{2}\right|^2[\delta(\omega+\omega_j)+\delta(\omega-\omega_j)]. \tag{29}$$

Figure 1 shows that the instrumental noise is ultimately divided into IP and Q channels, so that past the mixing (multiplying) stage

$$n_i^{(\mathrm{IP,Q})}(t)=n(t)e_R^{(\mathrm{IP,Q})}(t;\omega_0). \tag{30a}$$

Therefore,

$$n_i(t)=n_i(t)\cos\omega_0 t+n_i(t)\sin\omega_0 t=n_i^{\mathrm{IP}}(t)+n_i^{\mathrm{Q}}(t). \tag{30b}$$

It can be shown from properties of the Fourier transformation that the in-phase and quadrature power spectral densities of $n_i(t)$, $S_i^{\mathrm{IP}}(\omega)$ and $S_i^{\mathrm{Q}}(\omega)$, upon use of both $n_i(t)\cos\omega_0(t)$ and $n_i(t)\sin\omega_0 t$, are given by[27]

$$S_i^{\mathrm{IP}}(\omega)=S_i^{\mathrm{Q}}(\omega)=\frac{1}{4}[S(\omega+\omega_0)+S(\omega-\omega_0)]. \tag{31}$$

This result represents the expected intermediate noise component shift by ω_0 with pure sinusoidal modulation $e_R(t;\omega_0)$. Now using Eq. (29) in (31) and inserting the result in Eq. (28) yields

$$\begin{aligned}\overline{n_0^2(t)}&=\frac{1}{16}\lim_{\Delta\omega\to 0}\sum_{j=-\infty}^{\infty}C_j^2\int_{-\infty}^{\infty}|H(\omega)|^2[\delta(\omega+\omega_0+\omega_j)\\&\quad+\delta(\omega+\omega_0-\omega_j)+\delta(\omega-\omega_0+\omega_j)\\&\quad+\delta(\omega-\omega_0-\omega_j)]d\omega\\&=\frac{1}{16}\lim_{\Delta\omega\to 0}\sum_{j=-\infty}^{\infty}C_j^2[|H(-\omega_0-\omega_j)|^2\\&\quad+|H(-\omega_0+\omega_j)|^2+|H(\omega_0-\omega_j)|^2\\&\quad+|H(\omega_0+\omega_j)|^2].\end{aligned} \tag{32}$$

For narrow-band filters, such as the LIA filter with the transfer function Eq. (11) we may assume

$$H(-\omega_0\pm\omega_j)=H^*(\omega_0\mp\omega_j), \tag{33}$$

where starred quantities imply complex conjugation. This property can be readily proven for the $H(\omega_0)$ in Eq. (11) and helps simplify Eq. (32)

$$\overline{n_0^2(t)}=\frac{1}{8}\lim_{\Delta\omega\to 0}\sum_{j=-\infty}^{\infty}C_j^2[|H(\omega_0-\omega_j)|^2+|H(\omega_0+\omega_j)|^2]. \tag{34}$$

Henceforth, it is convenient to define the equivalent noise bandwidth (ENBW) $\Delta\omega_N=2\pi\Delta f_N$ as in Fig. 4. The ENBW is an ideal bandpass filter of constant gain $H(\omega_0)$ which delivers the same root-mean-square value of the noise signal power as the actual LIA output:

$$\Delta\omega_N=\frac{1}{|H(\omega_0)|^2}\int_0^{\infty}|H(\omega)|^2 d\omega, \tag{35a}$$

where

$$H(\omega_0)=\begin{cases}1; & \omega_0-(\Delta\omega_N/2)<\omega_0<\omega_0+(\Delta\omega_N/2)\\ 0; & \text{otherwise}\end{cases} \tag{35b}$$

The LIA output noise power is

$$\bar{P}_n=\overline{n_0^2(t)}\Delta\omega_j \quad [\mathrm{W}]. \tag{36}$$

Upon replacement of all the individual noise frequency bands $\Delta\omega_j=j\Delta\omega$ by suitable ENBWs, so that from Eq. (35a), one may write:

$$|H(\omega_j)|^2\Delta\omega_j=\int_0^\infty |H(\omega)|^2 d\omega. \tag{37}$$

One obtains for the output noise power from Eqs. (34), (36), and (37)

$$\bar{P}_n=\frac{1}{4}\int_0^\infty C^2(\omega)[|H(\omega_0-\omega)|^2+|H(\omega_0+\omega)|^2]d\omega. \tag{38}$$

The discrete Fourier coefficients C_j have also been replaced by continuous variables $C(\omega)$. In order to calculate $\bar{P}_n$, the instrumental noise is further assumed to be white, i.e., with uniform PSD over the entire frequency range. Denote the PSD as

$$S(\omega)=\frac{N}{2}\quad (\text{W/Hz}), \tag{39}$$

where the factor 1/2 is usually shown to indicate that half the power is associated with positive frequencies and half with negative frequencies. This model of noise has a physical basis on the thermal (or Johnson) noise of electronic circuits[28]

$$N=kT_e. \tag{40}$$

k is Boltzmann's constant and T_e is the equivalent noise temperature. This type of noise renders $C(\omega)$ independent of frequency in Eq. (38), which yields

$$\bar{P}_n=\frac{C^2}{4}\left(\int_0^\infty |H(\omega_0-\omega)|^2 d\omega+\int_0^\infty |H(\omega_0+\omega)|^2 d\omega\right). \tag{41}$$

Upon replacing the $S(\omega)$ in Eq. (29) by $N/2$ and taking the limit $\Delta\omega\to 0$ by replacing the summation by an integration over ω, letting $C_j=C$ (constant), gives

$$C^2=\frac{N}{2\pi}. \tag{42}$$

Finally, the IP or Q channel output noise power of the LIA becomes

$$\bar{P}_n=\left(\frac{N}{4\pi}\right)\Delta\omega_N\quad (\text{W}). \tag{43}$$

IV. PHOTOTHERMAL SNRs

A. Harmonic thermal-wave (FD) mode

For simplicity we shall consider a semi-infinite solid geometry as shown in Fig. 5. For harmonically modulated incident intensity [frequency domain (FD) mode]

$$Q(t)=\frac{Q_0}{2}[1+\cos(\omega_0 t)],$$

a simple heat conduction calculation with boundary conditions of temperature and heat flux continuity[29] gives for the thermal-wave field in the solid

$$T_s(x,t)=\frac{Q_0}{4k_s\sigma_s(1+b_{gs})}e^{-\sigma_s x+i\omega_0 t}. \tag{45}$$

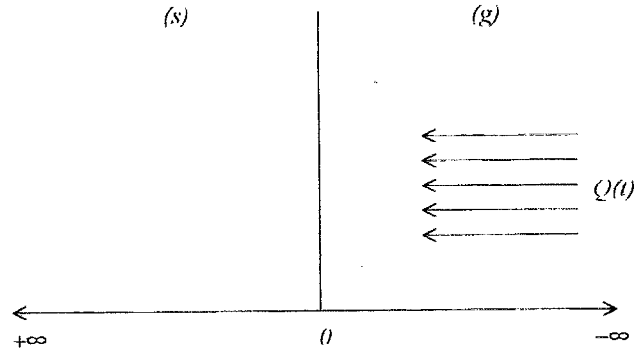

FIG. 5. One-dimensional, semi-infinite photothermal geometry. (s): solid, (g): gas, $Q(t)$: time-dependent incident photothermal intensity.

Here, k_s is the solid thermal conductivity; b_{gs} is the ratio of the thermal effusivities of gas and solid, $b_{gs}=e_g/e_s$; and $\sigma_s=(1+i)\sqrt{\omega_0/2\alpha_s}$, where α_s is the solid thermal diffusivity. Let us assume an experimental situation which is capable of monitoring the surface temperature oscillation of the solid directly, such as infrared photothermal radiometry[2,30]

$$T_s(0,t)=\frac{A}{\sqrt{\omega_0}}\cos\left(\omega_0 t-\frac{\pi}{4}\right)=f(t), \tag{46a}$$

where

$$A\equiv\frac{K_i Q_0}{4e_s(1+b_{gs})}, \tag{46b}$$

and K_i is an instrumental constant dependent on detection geometry. K_i does not change upon changing the input thermal modulation wave form of the system. In Eq. (46a) $T_s(0,t)$ may be identified as the input signal $f(t)$ to the LIA.

1. Digital LIA SNR

Computation of the fundamental Fourier coefficients of the FD surface temperature expression, Eq. (46a), via Eqs. [(17b) and (17c)] and insertion into the expression for the average output spectral power Eq. (21) with the average output noise power $\bar{P}_n$, Eq. (43), yields

$$a_1(\omega_0)=b_1(\omega_0)=\frac{A}{\sqrt{2\omega_0}}. \tag{47}$$

Therefore, for both IP and Q channels

$$\text{SNR}_d^{\text{FD}}(\omega_0)=\left(\frac{|A|^2}{8N\Delta f_N}\right)\frac{1}{\omega_0}. \tag{48}$$

The output power SNR in this mode decreases inversely proportional to the radiation intensity modulation frequency, a well-known experimental fact.

2. Analog LIA SNR

In this case calculation of a_{2n-1} and b_{2n-1} from Eqs. (17b) and (17c) shows that only the $n=1$ term survives, so that

$$f_{0T}^{(\text{IP,Q})}(\omega_0)=\frac{2}{\pi}\begin{pmatrix} b_1(\omega_0)\\ -a_1(\omega_0)\end{pmatrix}, \tag{49}$$

with $a_1 = b_1 = A/\sqrt{2}\omega_0$, as in Eq. (47). The results described in Eq. (49) are consistent with signal output considerations in the instrumental DLTS studies by Day *et al.*[24] and Auret[25] using the LIA rate window. If the instrumental noise consists of white Gaussian noise, the effect of the odd-harmonic response described by Eq. (26) is to increase the output noise power. Equation (38) must be modified[13] to include the noise power centered at $\omega=(2k-1)\omega_0$; $k=1, 2, 3,...$

$$\bar{P}_n=\frac{1}{4}\sum_{k=1}^{\infty}\int_0^{\infty}C_k^2(\omega)[|H(\omega_k-\omega)|^2+|H(\omega_k+\omega)|^2]d\omega. \tag{50}$$

The Fourier decomposition of the LIA square reference wave form, Eqs. (22) and (25), yields the following expression instead of Eq. (42)

$$C_k^2(\omega)=\frac{N}{2\pi(2k-1)^2}. \tag{51}$$

Therefore, for equal ENBWs at each odd harmonic $(2k-1)\omega_0$, a procedure similar to that which leads to Eq. (43) gives the total output noise power in both IP and Q channels of the analog LIA

$$\bar{P}_n=\left(\frac{N}{4\pi}\sum_{k=1}^{\infty}\frac{1}{(2k-1)^2}\right)\Delta\omega_N \quad \text{(W)}. \tag{52}$$

Finally, Eqs. (26a) and (52) lead to

$$\mathrm{SNR}_a^{\mathrm{FD}}(\omega_0)=\frac{1}{\omega_0}\left(\frac{|A|^2}{8N\Delta f_N}\right)\frac{1}{\sum_{k=1}^{\infty}\frac{1}{(2k-1)^2}}. \tag{53}$$

Given that

$$\sum_{k=1}^{\infty}\frac{1}{(2k-1)^2}=\frac{\pi^2}{8}=1.23, \tag{54}$$

it is seen that the 23% additional output noise power over the $\mathrm{SNR}_d^{\mathrm{FD}}(\omega_0)$ actually worsens the analog LIA SNR, in agreement with Meade's analysis (Ref. 11, Sec. 3.4). To overcome this setback, some manufacturers of analog lock-in amplifiers suggest the use of a separate bandpass filter located before the mixer/low-pass stage, centered on a particular undesirable input signal frequency, in order to remove the harmonic responses and thus the additional noise output.[11,14] Practically, the SNR improvement by use of front-end filters is insignificant, but the LIA dynamic reserve may be improved significantly. Figure 6 shows a comparison between digital and analog LIA photothermal FD data exhibiting the expected relative $\mathrm{SNR}(\omega_0)$ quality trends described in this section. The improvement in the amplitude SNR of the digital LIA is marginal, [Fig. 6(a)]. On the other hand, the improvement in phase SNR is substantial [Fig. 6(b)].

B. Rate-window (RW) photothermal mode

For an absolute and useful comparison of SNRs, the identical instrumental and sample configuration to that of Sec. IV A above is considered. In this mode, however, a time-gated optical pulse is incident on the sample surface of

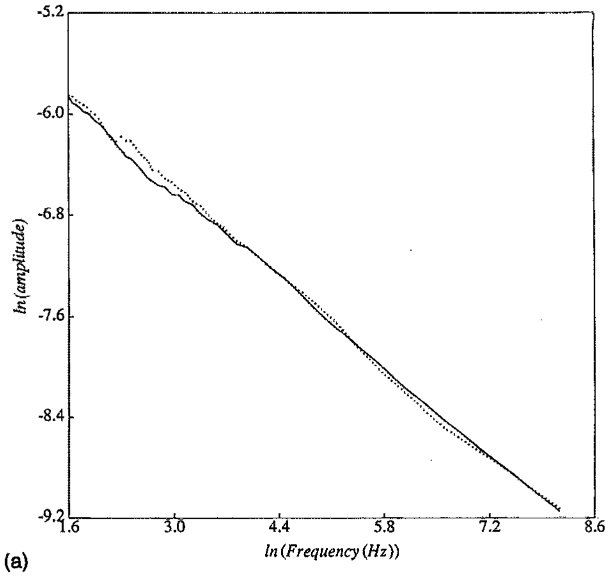

(a)

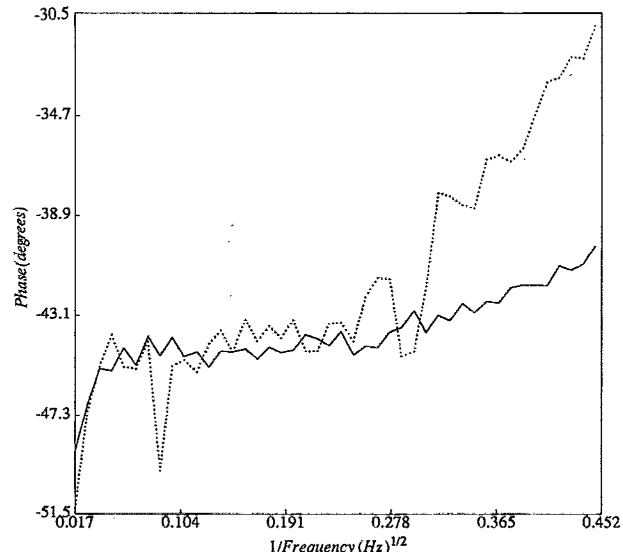

(b)

FIG. 6. Frequency-domain infrared photothermal radiometric scans of a semi-infinite solid using commercial digital and analog LIAs. (a) Amplitudes and (b) phases. (---) analog LIA; (—) digital LIA.

Fig. 5. The pulse is repetitive with period $T_0=2\pi/\omega_0$. The modulated incident intensity can be described by a rectangular pulse:

$$Q(t)=\begin{cases}Q_0; & 0<t<\tau_p\\ 0; & \tau_p<t<T_0\end{cases}. \tag{55}$$

A simple heat conduction calculation in the Laplace space with the same boundary conditions as the harmonic thermal-wave problem of Sec. IV A and initial condition $T_s(0,x)=0$ gives the TD counterpart of Eq. (46)

$$T_s(0,t)=\frac{4}{\sqrt{\pi}}A\times\begin{cases}\sqrt{t}; & 0\leq t\leq\tau_p\\ \sqrt{t}-\sqrt{t-\tau_p}; & \tau_p\leq t\leq T_0\end{cases}, \tag{56}$$

A is given in Eq. (46b). In view of the earlier comparison between digital and analog LIAs, we shall confine our attention to the former instrument, so as to avoid formalistic complications due to the presence of odd harmonics in the latter. Calculation of the fundamental Fourier coefficients of the function $f(t)=T_s(0,t)$ gives (see Appendix)

$$a_1(\omega_0)=\frac{4\omega_0 A}{\pi^{3/2}}\left(\int_0^{\tau_p}\sqrt{t}\cos(\omega_0 t)dt+\int_{\tau_p}^{T_0}(\sqrt{t}-\sqrt{t-\tau_p})\times\cos(\omega_0 t)dt\right)$$

$$=-\frac{4A}{\pi\sqrt{2\omega_0}}\left[S(2)-S\left(\sqrt{\frac{2}{\pi}(2\pi-\omega_0\tau_p)}\right)\times\cos(\omega_0\tau_p)-C\left(\sqrt{\frac{2}{\pi}(2\pi-\omega_0\tau_p)}\right)\sin(\omega_0\tau_p)+\sqrt{\frac{2}{\pi}(2\pi-\omega_0\tau_p)}\sin(\omega_0\tau_p)\cos(\omega_0\tau_p)\right]. \quad (57)$$

Also

$$b_1(\omega_0)=\frac{4\omega_0 A}{\pi^{3/2}}\left(\int_0^{\tau_p}\sqrt{t}\sin(\omega_0 t)dt+\int_{\tau_p}^{T_0}(\sqrt{t}-\sqrt{t-\tau_p})\sin(\omega_0 t)dt\right)$$

$$=\frac{4A}{\pi\sqrt{2\omega_0}}\left[C(2)-C\left(\sqrt{\frac{2}{\pi}(2\pi-\omega_0\tau_p)}\right)\cos(\omega_0\tau_p)+S\left(\sqrt{\frac{2}{\pi}(2\pi-\omega_0\tau_p)}\right)\sin(\omega_0\tau_p)+\sqrt{\frac{2}{\pi}(2\pi-\omega_0\tau_p)}\sin^2(\omega_0\tau_p)\right]. \quad (58)$$

Two rate-window photothermal modes are possible: pulse repetition period T_0 scan with fixed τ_p; and pulse duration τ_p scan with fixed T_0. In both scans extremes of the photothermal signal occur.[1,2] SNR comparisons with the FD mode are most easily made by considering the τ_p/T_0 ratio in the rate-window method which yields a SNR equal to that of the FD method. If $\omega_0\tau_p\ll 2\pi$, i.e., for $\tau_p\ll T_0$, the following approximations may be made

$$S\left(\sqrt{\frac{2}{\pi}(2\pi-\omega_0\tau_p)}\right)\simeq S(2), \quad (59)$$

$$C\left(\sqrt{\frac{2}{\pi}(2\pi-\omega_0\tau_p)}\right)\simeq C(2), \quad (60)$$

$$\cos(\omega_0\tau_p)\simeq 1; \quad \sin(\omega_0\tau_p)\simeq\omega_0\tau_p. \quad (61)$$

Therefore, Eq. (57) becomes for $\tau_p\ll T_0$

$$|a_1(\omega_0)|\simeq\frac{4A[2-C(2)]}{\pi\sqrt{2\omega_0}}(\omega_0\tau_p). \quad (62)$$

Since the instrumental configuration remains identical to the FD LIA method, the IP and Q channel output noise power $\bar{P}_n$ remains the same and is given by Eq. (43). Inserting[31] $C(2)\simeq 0.488$ in Eq. (62) one obtains

$$\mathrm{SNR}_d^{\mathrm{RW,IP}}(\omega_0)=\left(\frac{4[2-C(2)]}{\pi}\right)^2\left(\frac{|A|^2(\omega_0\tau_p)^2}{8N\Delta f_N}\right)\frac{1}{\omega_0}, \quad (63a)$$

$$=3.706(\omega_0\tau_p)^2\left(\frac{|A|^2}{8N\Delta f_N}\right)\frac{1}{\omega_0}. \quad (63b)$$

Equation (63) indicates that the output SNR from a rate-window photothermal experiment with fixed pulse duration and scanned repetition period or vice-versa is higher than the respective FD scan SNR, Eq. (48) when

$$3.706(\omega_0\tau_p)^2\geq 1\Rightarrow\tau_p\geq 8.267\times 10^{-2}T_0, \quad (64)$$

i.e., the in-phase rate-window method outperforms the conventional FD mode if the pulse duration is greater than 8.27% of the repetition period. The SNR advantage of the rate-window method over the FD method at common ω_0 increases with increasing modulation frequency [Eq. (63)]. This fact suggests that the rate-window approach should be favored in situations where fast photothermal detection is required, such as with responses of thin, thermally conducting layers. A similar calculation to the IP case may be carried out for the Q-channel of the LIA, giving from Eq. (60) in the limit $\omega_0\tau_p\ll 2\pi$

$$\mathrm{SNR}_d^{\mathrm{RW,Q}}(\omega_0)\simeq\left(\frac{4S(2)}{\pi}\right)^2\left(\frac{|A|^2(\omega_0\tau_p)^2}{8N\Delta f_N}\right)\frac{1}{\omega_0}, \quad (65a)$$

$$=0.191(\omega_0\tau_p)^2\left(\frac{|A|^2}{8N\Delta f_N}\right)\frac{1}{\omega_0}. \quad (65b)$$

The condition for the SNR advantage of the Q-channel rate-window scan over the FD method at the same frequency here is more stringent than the IP condition, yet easy to achieve experimentally

$$0.191(\omega_0\tau_p)^2\geq 1\Rightarrow\tau_p\geq 0.364T_0. \quad (66)$$

Figure 7 shows comparisons between infrared photothermal radiometric rate-window scans of T_0, quadrature channels, using digital and analog LIAs. The same semi-infinite Zr sample used in Fig. 6 was employed here. In Fig. 7(a) the strength of the signal was deliberately lowered by decreasing the intensity of the incident laser radiation. The improvement in the digital LIA SNR over the analog instrument is apparent. Figure 8 shows FD and rate-window infrared radiometric scans of a thin metallic strip. The data scatter of the FD phase curve [Fig. 8(a)] is more severe than that of the quadrature rate-window curve [Fig. 8(b)] especially in the low-to-middle frequency range. No theoretical curve was possible to fit to the data to calculate the thermal diffusivity from the FD experiment. On the other hand, both high-frequency (low T_0) and low-frequency (high T_0) regions of the rate-window scan exhibit acceptable SNR and theoretical curves were able to be fitted to the data for a range of thermal diffusivities. In turn, those values were used to draw theoretical fits through the experimental FD data. The mini-

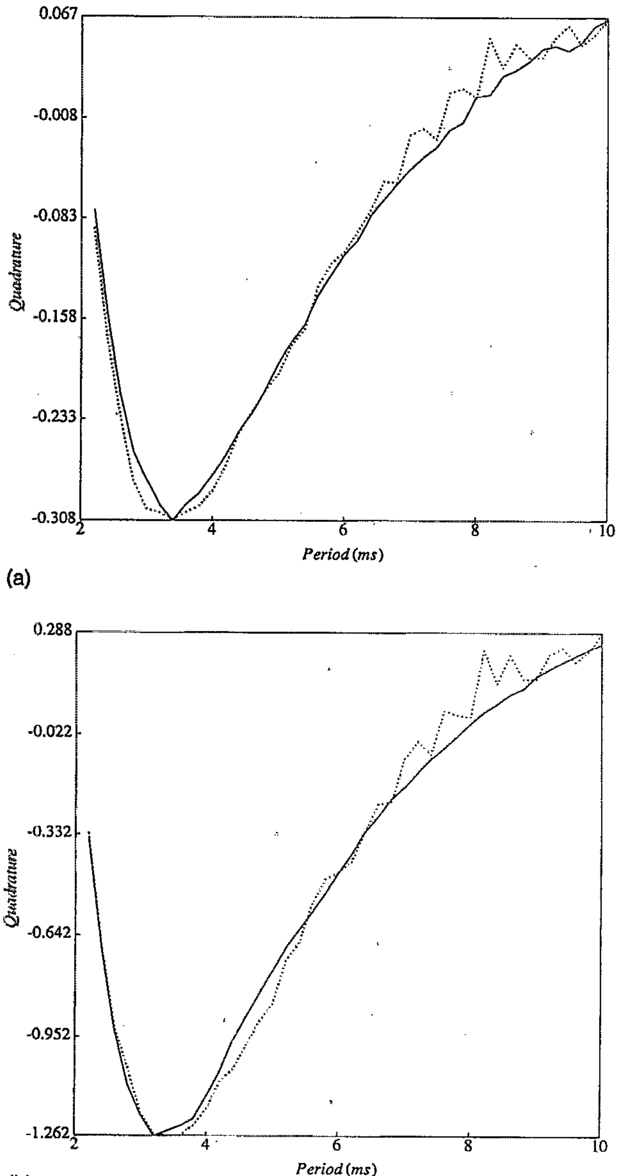

FIG. 7. Infrared photothermal radiometric response of a semi-infinite Zr sample. RW quadrature scan. (a) Low signal level corresponding to low incident laser irradiance; (b) high signal level corresponding to high incident irradiance. (---) analog LIA; (—) digital LIA. Pulse duration $\tau_p=2$ ms. LIA filter time constants $\tau_{RC}=1$ s.

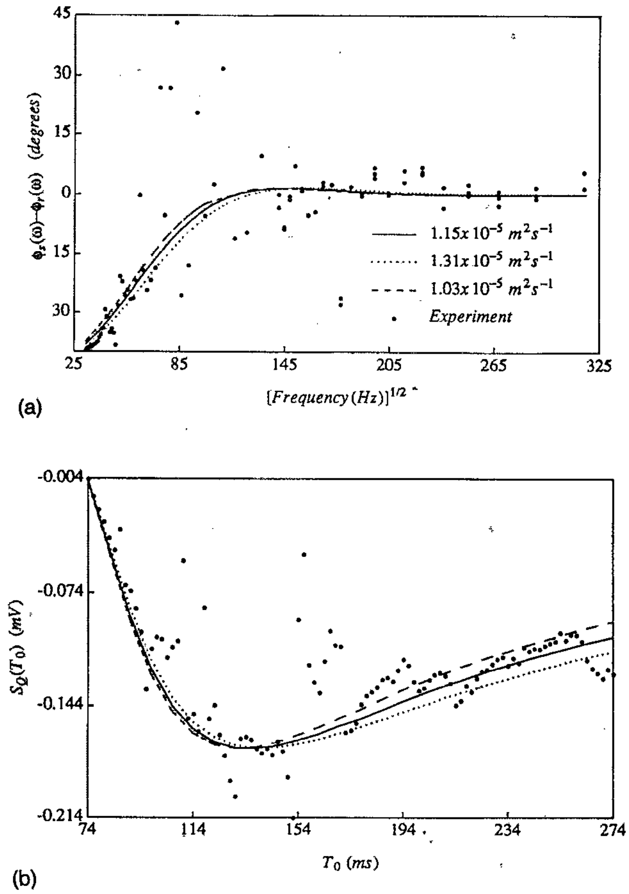

FIG. 8. (a) Experimental FD photothermal infrared radiometric phase data (filled circles) from a 25.4-μm thick metal foil, normalized to a semi-infinite reference sample, and the corresponding theoretical curves with thermal diffusivities 1.15×10^{-5} (solid), 1.31×10^{-5} (dots), and 1.03×10^{-5} (dashes) $m^2\,s^{-1}$. (b) Experimental Q-channel data (filled circles) from a rate-window T_0 scan with $\tau_p=73$ μs. The theoretical curves corresponding to the foregoing thermal diffusivities were drawn on this scan first and then used in (a).

mum ratio of the (fixed) τ_p to (scanned) T_0 was $(73\ \mu s/274\ \mu s)=0.266$, and the maximum ratio was 1. Therefore, condition (66) was satisfied for $T_0<203$ μs, although some deviation from the theory is expected due to the finite-thickness sample geometry. As a result, the rate-window SNR at 75 μs $(\tau_p/T_0=1)$ is much greater than the corresponding FD SNR at 13.5 kHz, i.e., 116.5 $\sqrt{\text{Hz}}$ on the abscissa of Fig. 8(a).

In the foregoing experimental examples, the SNRs of both FD and rate-window modes decrease substantially with increasing frequency, owing to their ω_0^{-1} dependence. If the pulse repetition period is fixed (i.e., ω_0 is fixed) and τ_p is scanned, then the relative in-phase SNR becomes

$$\rho\equiv\frac{\mathrm{SNR}_d^{\mathrm{RW,IP}}(\omega_0)}{\mathrm{SNR}_d^{\mathrm{FD}}(\omega_0)}=\left(\frac{4[2-C(2)]}{\pi}\right)^2(\omega_0\tau_p)^2$$

$$=3.706(\omega_0\tau_p)^2, \tag{67}$$

assuming $\omega_0\tau_p\ll1$, and

$$\rho=\left(\frac{4[S(2)+S(\sqrt{2})]}{\pi}\right)^2=1.81, \tag{68}$$

for $\tau_p=T_0/2$ (rate window with 50% duty cycle). Similar SNR advantages are enjoyed by the LIA Q channel as well.

The advantage of the pulse-duration-scanned rate window over FD photothermal measurements lies not only on the high SNR due to the rate-window process itself as shown in Eqs. (67) and (68), but also in comparison with the T_0-scanned rate window. This is so, because T_0 scanning is equivalent to increasing the modulation frequency, which compromises the photothermal SNR. To illustrate this important difference between the two rate-window scanning modes, consider the ratio of their SNRs from Eq. (63b) under the condition $\tau_p\ll T_0$

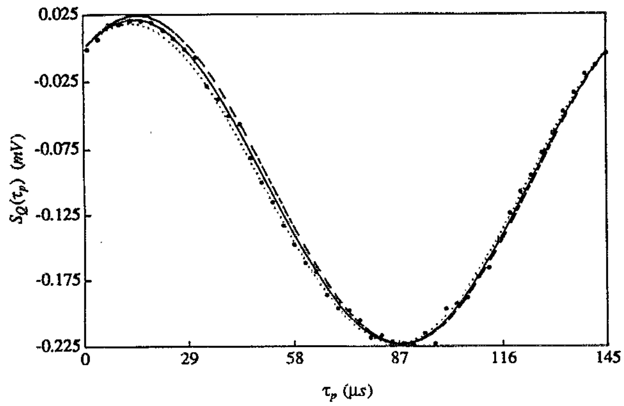

FIG. 9. Experimental Q-channel data (filled circles) from a rate-window τ_p scan of the 25.4-μm-thick metal foil of Fig. 8. The theoretical curves correspond to thermal diffusivities of 1.15×10^{-5} (solid), 1.31×10^{-5} (data), and 1.03×10^{-5} (dashes) $m^2\,s^{-1}$.

$$\rho\equiv\frac{\mathrm{SNR}_d^{\mathrm{RW,(IP\ or\ Q)}}(\tau_p,\omega_0^*)}{\mathrm{SNR}_d^{\mathrm{PW,IP}}(\tau_p^*,\omega_0)}=\frac{\omega_0}{\omega_0^*}\left(\frac{\omega_0^*\tau_p}{\omega_0\tau_p^*}\right)^2=\frac{T_0^*}{T_0}\left(\frac{(\tau_p/T_0^*)^2}{(\tau_p^*/T_0)^2}\right). \tag{69}$$

In Eq. (69) starred quantities denote fixed parameters; unstarred quantities denote scanned parameters. It can be seen that for the τ_p-scanned rate window, the ratio τ_p/T_0^* increases with increasing τ_p. Similarly, for the T_0-scanned rate window the ratio τ_p^*/T_0 increases with decreasing T_0. Assuming equal rates of increase, we obtain

$$\rho=T_0^*/T_0. \tag{70}$$

Note, that always $\rho\geq1$, the equality sign holding when both scans commence with the same τ_p and T_0. Then ρ quickly increases as τ_p increases (in constant T_0^* mode) or as T_0 decreases (in constant τ_p^* mode). Figure 9 shows the dramatic SNR enhancement in the Q-channel τ_p-scanned mode and should be compared to Fig. 8(b) which represents the T_0-scanned mode.

C. Pulsed and time-averaged photothermal (TD) mode

Pulsed photothermal (time-domain, TD) experiments are in widespread use owing to the ease of interpretation of the data and the ability to excite and monitor fast and ultrafast photothermal phenomena using pulsed lasers. The rate-window mode is principally a transient signal detection method using synchronous demodulation, therefore, the question of the SNR of the time-averaged pulsed photothermal method arises when direct comparison of the two measurement techniques is to be made. In this case the transient repetitive output signal $f_0(t)$ may be considered to be the result of averaging a continuous random variable time-dependent function. The mean value of the function $f_0(t)$ is[18]

$$E[f_0(t)]\equiv\overline{f_0(t)}=\int_{-\infty}^{\infty}f_0(t)p(f_0;t)df_0. \tag{71}$$

If m_i represents the number of times the function $f_0(t)$ takes on the value f_{0i} and n is the total number of times the transient experiment is repeated, then formally $p(f_0;t)$ is the limit as $n\to\infty$ of the ratio m_i/n; physically $p(f_0;t)$ is a probability density. The variance of $f_0(t)$ at any instant, t, is given by

$$\sigma_{f0}(t)=\sqrt{\overline{f_0^2(t)}-[\overline{f_0(t)}]^2}. \tag{72}$$

In a pulsed photothermal experiment the co-added repetitive pulses are not narrow-band filtered, since they are not transmitted through a LIA. Assuming stationary Gaussian white noise dominating all other types of noise, with PSD given by Eq. (39), the mean-square value of the noise signal can be expressed as in Eq. (28), which takes on the particularly simple form

$$\overline{n_0^2(t)}=\frac{N}{4\pi}\int_{-\infty}^{\infty}|H(\omega)|^2d\omega. \tag{73}$$

$H(\omega)$ denotes the transfer function of the dominant frequency-limiting mechanism of the experiment, which acts as a distributed bandpass filter. The probability density function of band-limited Gaussian white noise is known to be[18]

$$p(n_0)=\frac{1}{\sqrt{2\pi NB}}\,e^{-n_0^2/2NB}, \tag{74}$$

where B is the effective bandwidth

$$B=\frac{W}{2\pi}\ \text{(Hz)}. \tag{75}$$

Here, W is the entire bandwidth of the experimental frequency spectrum. For repetitive pulsed photothermal transients with repetition period T_0, the bandwidth is $|\omega|<\omega_0=2\pi/T_0$, which yields

$$B=\frac{1}{T_0}=\frac{\omega_0}{2\pi}. \tag{76}$$

The output signal is mixed with white Gaussian noise of zero mean value

$$r_0(t)=f_0(t)+n_0(t), \tag{77}$$

where, according to Eqs. (71) and (74)

$$\overline{n_0^2(t)}=\int_{-\infty}^{\infty}n_0^2p(n_0)dn_0=NB. \tag{78}$$

Presently, let $f_0(t)$ be given by the photothermal response of a semi-infinite solid to a rectangular pulse $Q(t)$. This response is described by Eq. (56). Given that $r_0(t)$ is considered a random function over an ensemble with Gaussian probability density, that probability density may be described using Eq. (74) with $n_0=r_0-f_0$

$$p(r_0;f_0)=\frac{1}{\sqrt{2\pi NB}}\,e^{-(r_0-f_0)^2/2NB}. \tag{79}$$

After infinite time averaging of the repetitive transient signals, the mean value of the resulting TD signal will be

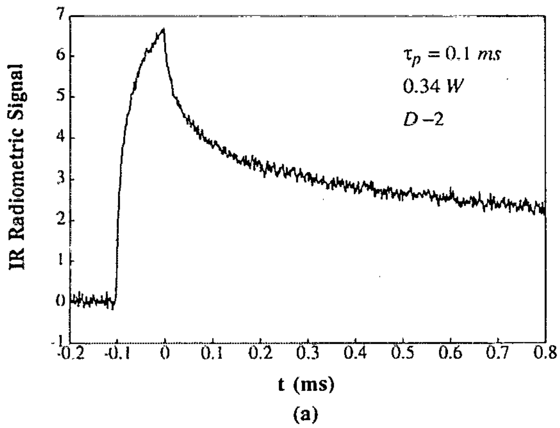

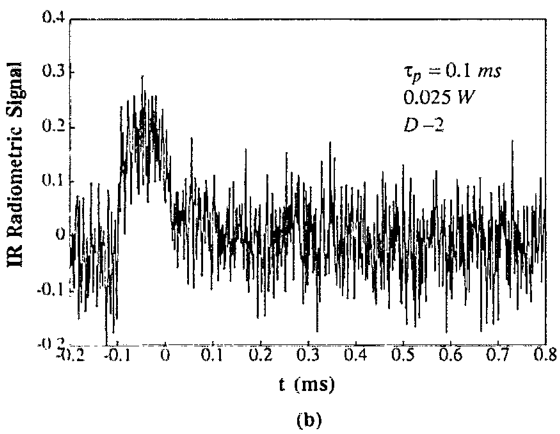

FIG. 10. Backscattered infrared photothermal radiometric TD signal from a diamond sample averaged over $N=5000$ samples. Pulse duration $\tau_p=0.1$ ms. Laser power $Q_0=0.34$ W (a); $Q_0=25$ mW (b).

$$\overline{r_0(t)}=\int_{-\infty}^{\infty} r_0 p(r_0;f_0)dr_0=f_0(t), \tag{80}$$

where Eq. (79) was used for the calculation.

The system output noise will result in a variance which determines the SNR. This variance is given by Eq. (72) upon replacing f_0 by r_0

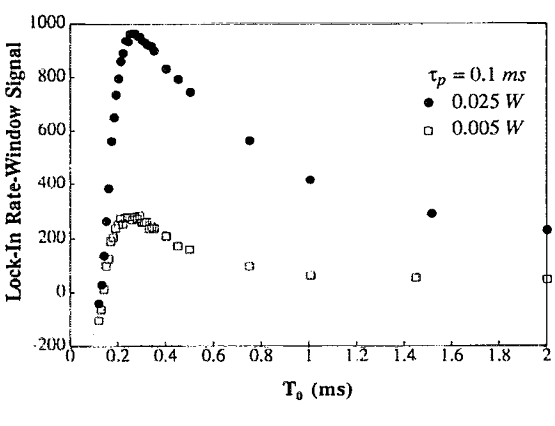

FIG. 11. Analog LIA IP-channel infrared photothermal radiometric rate-window signals from the diamond of Fig. 10. Two scans were performed with $\tau_p=0.1$ ms and $Q_0=25$ mW (black dots) and 5 mW (squares).

$$\sigma_{r_0}^2=\int_{-\infty}^{\infty} r_0^2 p(r_0;f_0)dr_0-\left(\int_{-\infty}^{\infty} r_0 p(r_0;f_0)dr_0\right)^2$$
$$=[NB+f_0^2(t)]-f_0^2(t)=NB. \tag{81}$$

From Eqs. (80) and (81) we conclude (see also Ref. 11, Appendix 2)

$$\mathrm{SNR}^{\mathrm{TD}}(t)=\frac{\overline{r_0^2(t)}}{\overline{n_0^2(t)}}=\frac{f_0^2(t)}{\sigma_{r_0}^2}=\frac{T_s^2(0,t)}{NB}. \tag{82}$$

Over the entire repetition cycle, the output power SNR is given by Eq. (1) as follows

$$\mathrm{SNR}^{\mathrm{TD}}(T_0)=\frac{\frac{1}{T_0}\int_0^{T_0}T_s^2(0,t)dt}{NB}. \tag{83}$$

Now, calculation of the integral in the numerator using Eq. (56) and Ref. 32, entries 2.261 and 2.262.3 gives

$$\mathrm{SNR}^{\mathrm{TD}}(T_0)=\left[T_0+\frac{1}{2}\frac{\tau_p^2}{T_0}-\tau_p-\sqrt{T_0^2-\tau_pT_0}\left(1-\frac{\tau_p}{2T_0}\right)\right.$$
$$\left.+\frac{\tau_p^2}{2T_0}\ln\left(\sqrt{\frac{T_0}{\tau_p}}+\sqrt{\frac{T_0}{\tau_p}-1}\right)\right]\left(\frac{16A^2}{\pi NB}\right). \tag{84}$$

This SNR increases with increasing τ_p, as expected since the total energy imparted into the sample increases. For a direct comparison with the rate-window SNR, Eq. (63), consider the case of a short laser pulse, such that $\tau_p \ll T_0$. Using the approximations

$$(T_0^2-\tau_pT_0)^{1/2}\simeq T_0\left(1-\frac{\tau_p}{2T_0}\right), \tag{85}$$

and

$$\tau_p^2\ln\left(\sqrt{\frac{T_0}{\tau_p}}+\sqrt{\frac{T_0}{\tau_p}-1}\right)\simeq\tau_p^2\ln\left(2\sqrt{\frac{T_0}{\tau_p}}\right)\simeq\frac{\tau_p^{5/2}}{2\sqrt{T_0}}, \tag{86}$$

and keeping in mind Eq. (76), we obtain

$$\mathrm{SNR}^{\mathrm{TD}}(\tau_p\ll T_0)\simeq\frac{4A^2}{\pi NB}\left(\frac{\tau_p^2}{T_0}\right)=\frac{4A^2\tau_p^2}{\pi N};\quad (A=|A|^2). \tag{87}$$

Finally, using Eqs. (63b) and (87) the relative SNR for short optical pulses $\tau_p \ll T_0$ becomes

$$\frac{\mathrm{SNR}_d^{\mathrm{RW,IP}}(\omega_0)}{\mathrm{SNR}^{\mathrm{TD}}(T_0)}=2.29\left(\frac{\omega_0}{\Delta\omega_N}\right)\gg 1. \tag{88}$$

This ratio is normally much greater than one, due to the extremely narrow ENBWs afforded by LIAs (typically $\Delta f_N \simeq 0.01$ Hz at $f_0=\omega_0/2\pi=10$ kHz).[17] This advantage of rate-window detection over the co-added transient method is demonstrated experimentally in Figs. 10 and 11. Figure 10 shows a photothermal infrared radiometric transient measured from a diamond sample using a finite duration laser pulse ($\tau_p=0.1$ ms) and two levels of incident irradiance. The low incident laser power is only 25 mW [Fig. 10(b)].

Several thousand repetitive signal transients were co-added. Figure 11 shows the LIA rate-window scans measured with the same τ_p and the incident laser power of Fig. 10(b), as well as an even lower power of only 5 mW. No transient signal could be registered in the transient scope in this latter case, even after the co-addition and averaging of several thousand pulses. Comparison of Figs. 10(b) and 11 clearly indicates the superior SNR of the LIA rate-window method.

ACKNOWLEDGMENTS

The support of the Manufacturing Research Corporation of Ontario (MRCO) and the Natural Sciences and Engineering Research Council of Canada (NSERC) is gratefully acknowledged. The assistance of M. Munidasa and F. Funak with the production of some figures used in this report is also acknowledged. Furthermore, the author wishes to acknowledge valuable discussions and comments on the manuscript by Professor S. Cova, Politecnico di Milano.

APPENDIX: CALCULATION OF FUNDAMENTAL FOURIER COEFFICIENTS FOR THE PHOTOTHERMAL LIA RESPONSE OF A SEMI-INFINITE SOLID TO A TIME-GATED RECTANGULAR OPTICAL PULSE

If the pulse duration is τ_p and the pulse repetition period is $T_0=2\pi/\omega_0$, Eq. (56) gives the transient response $T_s(0,t)$ of a semi-infinite solid surface. The output spectral power of the LIA filter is proportional to $|a_1|^2$ and $|b_1|^2$ for the IP and Q channels, respectively, where

$$\begin{pmatrix} a_1(\omega_0) \\ b_1(\omega_0) \end{pmatrix} = \frac{\omega_0}{\pi} \int_0^{T_0} T_s(0,t) \begin{pmatrix} \cos(\omega_0 t) \\ \sin(\omega_0 t) \end{pmatrix} dt. \tag{A1}$$

Now, we may write, using Eq. (57)

$$a_1(\omega_0)=\frac{4\omega_0 A}{\pi^{3/2}} \left(\int_0^{T_0} \sqrt{t} \cos(\omega_0 t)dt - \int_{\tau_p}^{T_0} \sqrt{t-\tau_p} \cos(\omega_0 t)dt \right). \tag{A2}$$

Integration by parts yields

$$I_1(\omega_0) \equiv \int_0^{T_0} \sqrt{t} \cos(\omega_0 t)dt = -\frac{1}{2\omega_0^{3/2}} \int_0^{2\pi} \frac{\sin x}{\sqrt{x}} dx,$$

or, using the auxiliary Fresnel integrals (Ref. 31, entries 7.3.3 and 7.3.4)

$$S_2(x)=\frac{1}{\sqrt{2\pi}} \int_0^x \frac{\sin y}{\sqrt{y}} dy, \tag{A3a}$$

$$C_2(x)=\frac{1}{\sqrt{2\pi}} \int_0^x \frac{\cos y}{\sqrt{y}} dy, \tag{A3b}$$

which may also be written in terms of the basic Fresnel integrals (Ref. 31, entries 7.3.7 and 7.3.8),

$$S(x)=S_2\left(\frac{\pi}{2} x^2\right), \tag{A4a}$$

$$C(x)=C_2\left(\frac{\pi}{2} x^2\right), \tag{A4b}$$

we obtain for I_1

$$I_1(\omega_0)=-\sqrt{\frac{\pi}{2\omega_0^3}} S_2(\sqrt{2\pi}). \tag{A5}$$

Also defining

$$I_2(\omega_0) \equiv \int_{\tau_p}^{T_0} \sqrt{t-\tau_p} \cos(\omega_0 t)dt, \tag{A6}$$

changing the integration variable to $y=t-\tau_p$, and expanding the resulting $\cos[\omega_0(y+\tau_p)]$ gives

$$I_2(\omega_0)=-\sqrt{\frac{\pi}{2\omega_0^3}} S_2(\sqrt{2\pi-\omega_0\tau_p})\cos(\omega_0\tau_p) - I_3(\omega_0)\sin(\omega_0\tau_p) \tag{A7}$$

where

$$I_3(\omega_0) \equiv \int_0^{T_0-\tau_p} \sqrt{y} \sin(\omega_0 y)dy. \tag{A8}$$

Integration by parts of $I_3(\omega_0)$ yields

$$I_3(\omega_0)=-\frac{1}{\omega_0} \sqrt{T_0-\tau_p} \cos(\omega_0\tau_p) + \sqrt{\frac{\pi}{2\omega_0^3}} C_2(\sqrt{2\pi-\omega_0\tau_p}). \tag{A9}$$

Inserting the results of Eqs. (A5), (A7), and (A9) into Eq. (A2) gives

$$a_1(\omega_0) = -\frac{4A}{\pi\sqrt{2\omega_0}} \Big[S_2(\sqrt{2\pi}) - S_2(\sqrt{2\pi-\omega_0\tau_p})\cos(\omega_0\tau_p) - C_2(\sqrt{2\pi-\omega_0\tau_p})\sin(\omega_0\tau_p) + \left(\frac{2}{\pi}\right)^{1/2} \sqrt{2\pi-\omega_0\tau_p} \sin(\omega_0\tau_p)\cos(\omega_0\tau_p) \Big].$$

Finally, using the Fresnel integrals proper via Eqs. (A4), we obtain Eq. (59). Similarly,

$$b_1(\omega_0)=\frac{4\omega_0 A}{\pi^{3/2}} \left(\int_0^{T_0} \sqrt{t} \sin(\omega_0 t)dt - \int_{\tau_p}^{T_0} \sqrt{t-\tau_p} \sin(\omega_0 t)dt \right). \tag{A11}$$

Integration by parts yields

$$I_4(\omega_0) \equiv \int_0^{T_0} \sqrt{t} \sin(\omega_0 t)dt = \sqrt{\frac{\pi}{2\omega_0^3}} C_2(\sqrt{2\pi}). \tag{A12}$$

Also:

$$I_5(\omega_0) \equiv \int_{\tau_p}^{T_0} \sqrt{t-\tau_p} \sin(\omega_0 t)dt. \tag{A13}$$

Similar treatment to the integral $I_2(\omega_0)$ gives

$$I_5(\omega_0) = \sqrt{\frac{\pi}{2\omega_0^3}}\, C_2(\sqrt{2\pi - \omega_0 \tau_p})\cos(\omega_0 \tau_p)$$

$$+ I_6(\omega_0)\sin(\omega_0 \tau_p), \tag{A14}$$

where

$$I_6(\omega_0) \equiv \int_0^{T_0 - \tau_p} \sqrt{y}\, \cos(\omega_0 y)\, dy. \tag{A15}$$

Integration by parts yields

$$I_6(\omega_0) = -\frac{1}{\omega_0}\sqrt{T_0 - \tau_p}\, \sin(\omega_0) - \sqrt{\frac{\pi}{2\omega_0^3}} S_2(\sqrt{2\pi - \omega_0 \tau_p}). \tag{A16}$$

Inserting Eqs. (A12)–(A16) into Eq. (A11) gives

$$b_1(\omega_0) = \frac{4A}{\pi\sqrt{2\omega_0}} \Bigg[C_2(\sqrt{2\pi}) - C_2(\sqrt{2\pi - \omega_0 \tau_p})\cos(\omega_0 \tau_p)$$

$$+ S_2(\sqrt{2\pi - \omega_0 \tau_p})\sin(\omega_0 \tau_p)$$

$$+ \left(\frac{2}{\pi}\right)^{1/2} \sqrt{2\pi - \omega_0 \tau_p}\, \sin^2(\omega_0 \tau) \Bigg]. \tag{A17}$$

Use of the Fresnel integrals, Eqs. (A4), finally yields Eq. (60). For computational purposes the Taylor series expansions may be used for small values of the argument (Ref. 31, entries 7.3.11 and 7.3.13)

$$C(x) = \sum_{n=0}^{\infty} (-1)^n \frac{(\pi/2)^{2n}}{(2n)!(4n+1)} x^{4n+1} \tag{A18}$$

and

$$S(x) = \sum_{n=0}^{\infty} (-1)^n \frac{(\pi/2)^{2n+1}}{(2n+1)!(4n+3)} x^{4n+3} \tag{A19}$$

Asymptotically,

$$C(x) \sim S(x) \sim \frac{1}{2} \text{ as } x \to \infty. \tag{A20}$$

[1] A. Mandelis and Z. Chen, Rev. Sci. Instrum. **63**, 2977 (1992).
[2] Z. Chen and A. Mandelis, Phys. Rev. B **46**, 13526 (1992).
[3] Z. H. Chen, R. Bleiss, A. Mandelis, A. Buczkowski, and F. Shimura, J. Appl. Phys. **73**, 5043 (1993).
[4] A. Mandelis, R. Bleiss, and F. Shimura, J. Appl. Phys. **74**, 3431 (1993).
[5] M. Munidasa and A. Mandelis, Rev. Sci. Instrum. **65**, 2344 (1994).
[6] G. L. Miller, J. V. Ramirez, and D. A. H. Robinson, J. Appl. Phys. **46**, 2638 (1975).
[7] D. M. Munroe, *The Heterodyning Lock-in Amplifier*, Ithaco Corp. Tech. Bull. 1973 (unpublished).
[8] L. E. Franks and I. W. Sandberg, Bell Syst. Tech. J. **39**, 1321 (1960).
[9] S. F. Carter and E. A. Faulkner, Electron. Lett. **3**, 381 (1977).
[10] D. P. Blair and P. H. Sydenham, J. Phys. E: Sci. Instrum. **8**, 621 (1975).
[11] M. L. Meade, *Lock-in amplifiers: principles and applications*, IEEE Electrical Measurement Series 1 (Peregrinus, Stevenage, Herts, England, 1983).
[12] T. H. Wilmshurst, *Signal Recovery from Noise in Electronic Instrumentation*, 2nd ed. (Adam Hilger, Bristol, 1990).
[13] S. Cova and A. Longoni, Chem. Analysis **50** (1979), Chap. 7.
[14] D. M. Munroe, *A Lock-in Amplifier Primer*, EG & G Princeton Applied Research Technical Publication T459, 1986; also: *Introduction to Lock-in Amplifiers*, Technical Note 115: Princeton Applied Research Corp. 1974 (unpublished).
[15] S. G. Letzter, Electron. Des. **21**, 104 (1974).
[16] Brookdeal Electronics, *Introduction to Lock-in Amplifiers* Bracknell, England, Technical Note 115 (unpublished).
[17] Stanford Research Systems Model SR850 DSP Lock-In Amplifier Manual, Sect. 3, 1992–1993 (unpublished).
[18] B. P. Lathi, *Random Signals and Communication Theory* (International Textbook, Scranton, PA, 1968), Chaps. 1 and 4.
[19] F. T. Arecchi, E. Gatti, and A. Sona, Rev. Sci. Instrum. **37**, 942 (1966).
[20] E. D. Morris, Jr. and H. S. Johnston, Rev. Sci. Instrum. **39**, 620 (1968).
[21] R. L. Chase, Rev. Sci. Instrum. **42**, 319 (1971).
[22] S. Cova, A. Longoni, and I. Freitas, Rev. Sci. Instrum. **50**, 296 (1979).
[23] A. Papoulis, *The Fourier Integral and its Applications* (McGraw-Hill, New York, 1962).
[24] D. S. Day, M. Y. Tsai, B. G. Streetman, and D. V. Lang, J. Appl. Phys. **50**, 5093 (1979).
[25] F. D. Auret, Rev. Sci. Instrum. **57**, 1597 (1986).
[26] B. P. Lathi, *Modern Digital and Analog Communication Systems* (Holt, Rinehart and Winston, New York, 1983), Chap. 2.10.
[27] B. P. Lathi, *Communication Systems* (Wiley, New York, 1968), Chap. 2.8.
[28] S. Haykin, *An Introduction to Analog and Digital Communications* (Wiley, New York, 1989), p. 160.
[29] H. S. Carslaw and J. C. Jaeger, *Conduction of Heat in Solids*, 2nd ed. (Oxford University Press, Oxford, 1965), Chap. 2.6.
[30] W. P. Leung and A. C. Tam, J. Appl. Phys. **56**, 153 (1984).
[31] M. Abramowitz and A. Stegun, *Handbook of Mathematical Functions*, 9th ed. (National Bureau of Standards, Washington, DC 1970).
[32] I. S. Gradshteyn and I. M. Ryzhik, *Table of Integrals, Series, and Products* (Academic, New York, 1980).